

Numerical and Asymptotical Study of Three-Dimensional Wave Packets in a Compressible Boundary Layer

Eric Forgoston ^{*}, Michael Viergutz [†] and Anatoli Tumin[‡]

The University of Arizona, Tucson, Arizona 85721

A three-dimensional wave packet generated by a local disturbance in a two-dimensional hypersonic boundary layer flow is studied with the aid of the previously solved initial-value problem. The solution can be presented as a sum of modes consisting of continuous and discrete spectra of temporal stability theory. Two discrete modes, known as Mode S and Mode F, are of interest in high-speed flows since they may be involved in a laminar-turbulent transition scenario. The continuous and discrete spectra are analyzed numerically for a hypersonic flow. A comprehensive study of the spectrum is performed, including Reynolds number, Mach number and temperature factor effects. A specific disturbance consisting of an initial temperature spot is considered, and the receptivity to this initial temperature spot is computed for both the two-dimensional and three-dimensional cases. Using the analysis of the discrete and continuous spectrum, the inverse Fourier transform is computed numerically. The two-dimensional inverse Fourier transform is calculated for Mode F and Mode S. The Mode S result is compared with an asymptotic approximation of the Fourier integral, which is obtained using a Gaussian model as well as the method of steepest descent. Additionally, the three-dimensional inverse Fourier transform is found using an asymptotic approximation. Using the inverse Fourier transform computations, the development of the wave packet is studied, including effects due to Reynolds number, Mach number and temperature factor.

I. Introduction

It is important to study the transition from laminar flow to turbulent flow in hypersonic boundary layers due to the role it will have in the development of future vehicles operating at hypersonic speeds. Aerodynamic heating on an aircraft changes dramatically when the laminar flow becomes turbulent. Since aerodynamic heating affects the choice of materials used for protecting the vehicle - and therefore the weight of the vehicle - the laminar-turbulent transition process must be understood.

The transition process from laminar to turbulent flow in hypersonic boundary layers has been studied for many years. However, because experimental conditions are so severe in hypersonic wind tunnels, our understanding of this phenomena is still very poor compared with the low speed case. Because of high levels of free-stream noise, it is difficult to perform experiments with controlled disturbances. Unlike the low speed case, it is difficult to design perturbers that can generate high-frequency artificial disturbances of individual modes. Instead, wave trains and wave packets are used in the experiment. Therefore, interpretation of experimental data is not straightforward, and this issue leads to the need for close coordination between theoretical modeling and experimental design and testing.

Several methods for excitation of artificial disturbances in a hypersonic boundary layer are available.¹⁻⁴ These methods could be used to generate either two-dimensional (2D) or three-dimensional (3D) wave packets of a broad frequency band. Additionally, due to advances in computational fluid dynamics, it is possible to perform reliable direct numerical simulations of laminar-turbulent transition to better understand the mechanisms leading to hypersonic boundary layer transition.⁵⁻¹¹

^{*}Graduate Student, Program in Applied Mathematics. Member AIAA.

[†]Graduate Student, Mechanical Engineering.

[‡]Professor, Department of Aerospace and Mechanical Engineering. Associate Fellow AIAA.

Accompanying these experiments, both wind tunnel and numerical, should be theoretical modeling and studies of the development of perturbations in hypersonic boundary layers.

The dynamics of the flow transition depend on the instability of small perturbations excited by external sources. When one investigates the stability of flows, the motion is decomposed into the basic flow whose stability is to be examined, and a superimposed perturbation. Linearization of the governing equations leads to a system of PDEs. With a parallel flow approximation, Fourier and Laplace transforms can be used to transform these PDEs into a system of ODEs. This set of ODEs, along with the associated boundary conditions, can be recast as an eigenvalue problem.

At this stage, the eigenmodes can be analyzed within the scope of a spatial theory or a temporal theory. For the spatial analysis, the frequency of the perturbation is prescribed to be real-valued, and one solves the eigenvalue problem for the complex-valued wave number. For the temporal analysis, one prescribes the wave number to be real-valued, and solves the eigenvalue problem for the complex-valued frequency. Consideration of the PDEs within the scope of the physical problem one is interested in will dictate the choice of temporal or spatial theory. The signaling problem¹² is the physical problem associated with the spatial stability theory. The initial-value problem¹³ is the physical problem associated with the temporal stability theory.

In 1979, Gustavsson¹³ formulated and solved the viscous 2D initial-value problem for incompressible boundary layer flows. In 1981, Salwen and Grosch¹⁴ derived a biorthogonality relation between the solution of the Orr-Sommerfeld equation and its adjoint within the framework of the temporal stability theory. Additionally, they showed that the set of eigenfunctions formed a complete set, and therefore, a solution of the initial-value problem for disturbances in a boundary layer could be expanded as a linear combination of those eigenfunctions.

In the early 2000s, Fedorov and Tumin¹⁵ analyzed a 2D initial-value problem in a compressible boundary layer with the use of Fourier and Laplace transforms. However, they did not compute the inverse Fourier transform for the wave packet. Forgoston and Tumin¹⁶ extended the work of Ref. 15 by solving the initial-value problem for three-dimensional (3D) wave packets. Once again, the inverse Fourier transform was not computed. Later, Forgoston and Tumin¹⁷ considered the specific disturbance of an initial temperature spot. The receptivity to the temperature spot was found for both the 2D and 3D cases. They computed the 2D inverse Fourier transform for two discrete modes, Mode F and Mode S, and the computed inverse Fourier transform for Mode S was compared with an asymptotic approximation of the Fourier integral. Although the approximation was generally quite good, there was a serious discrepancy at the wave packet “tails.”

Mack^{18,19} used linear stability theory to perform extensive studies of the behavior of 2D and 3D instability modes for both the temporal and spatial problems. In particular, he discovered that for compressible flows, higher acoustic instability modes exist along with the first mode. However, even though the behavior of these modes is understood, the mechanism by which the modes are generated (receptivity problem) is still a subject of research. Throughout the 1980s, 1990s and 2000s, Fedorov and colleagues discovered many results involving the receptivity of high speed flows. One can find a complete bibliography in Refs. 20, 21, 22 and 23.

Particularly, this spatial analysis of the 2D instability modes in hypersonic flows revealed the following: (1) in the region of the leading edge, Mode F and Mode S are synchronized with fast and slow acoustic waves respectively; (2) at a downstream location, Mode F is synchronized with the entropy and vorticity waves; (3) further downstream, Mode F and Mode S could also become synchronized.²⁴ It is important to understand these features due to the role they may have in the transition process. Later on, similar features of Mode F and Mode S were seen in the 2D temporal problem.¹⁵

For the 3D initial-value problem, Mode F and Mode S were analyzed within the framework of the temporal stability theory in Ref. 16 for one particular choice of parameters, and the following features were revealed: (1) the synchronism of Mode S with acoustic waves at a streamwise wave number $\alpha \rightarrow 0$ is primarily two-dimensional; (2) at high angles of disturbance propagation, Mode F is no longer synchronized with entropy and vorticity waves; (3) at high angles of disturbance propagation, the synchronism between Mode S and Mode F is not accompanied by a Mode S instability, and at even higher angles of disturbance propagation, Mode S and Mode F are not synchronized. These discrete modes were later analyzed within the framework of the spatial stability theory in Ref. 23, and similar results were found. A complete understanding of the features of the spectrum is needed to compute the inverse Fourier transform.

For clarity of the discussion, the previously solved initial-value problem for a 3D wave packet in a hypersonic boundary layer flow is briefly reviewed. The objective is to reconsider the specific disturbance of an initial temperature spot. The previously computed 2D inverse Fourier transform is compared to an

improved asymptotic approximation (one that resolves the discrepancy located at the wave packet “tails”). Additionally, the 3D inverse Fourier transform is found using the improved asymptotic approximation.

Furthermore, since the receptivity problem was not understood during the time of Mack’s investigations, and since it has not yet been done, it is worth revisiting the eigenmode analysis. Included is a comprehensive study of the effect of Reynolds number, Mach number and temperature factor on the spectrum and on the development of wave packets.

II. Problem Formulation

A 3D parallel boundary layer flow of a calorically perfect gas is considered. At the initial time, $t = 0$, a 3D localized disturbance is introduced into the flow. The problem is to describe the downstream evolution of the perturbation. The streamwise, normal and spanwise spatial coordinates are given respectively by x , y and z . Additionally, we denote u , v and w to be respectively the streamwise, normal and spanwise velocity disturbances, and θ , π , ρ and μ to be respectively the temperature, pressure, density and viscosity disturbances. Letting

$$\mathbf{A} = (u, \partial u / \partial y, v, \pi, \theta, \partial \theta / \partial y, w, \partial w / \partial y)^T \quad (1)$$

be the disturbance vector function, where “T” stands for “transpose”, it is possible to rewrite the system of linearized, dimensionless governing equations (continuity equation, x , y and z momentum equations, and energy equation) in the following matrix operator form:

$$\begin{aligned} \frac{\partial}{\partial y} \left(\mathbf{L}_0 \frac{\partial \mathbf{A}}{\partial y} \right) + \frac{\partial \mathbf{A}}{\partial y} = & \mathbf{H}_{10} \frac{\partial \mathbf{A}}{\partial t} + \mathbf{H}_{11} \mathbf{A} + \mathbf{H}_2 \frac{\partial \mathbf{A}}{\partial x} + \mathbf{H}_3 \frac{\partial^2 \mathbf{A}}{\partial x \partial y} + \mathbf{H}_4 \frac{\partial^2 \mathbf{A}}{\partial x^2} + \\ & \mathbf{H}_5 \frac{\partial \mathbf{A}}{\partial z} + \mathbf{H}_6 \frac{\partial^2 \mathbf{A}}{\partial x \partial z} + \mathbf{H}_7 \frac{\partial^2 \mathbf{A}}{\partial y \partial z} + \mathbf{H}_8 \frac{\partial^2 \mathbf{A}}{\partial z^2}, \end{aligned} \quad (2)$$

where \mathbf{L}_0 , \mathbf{H}_{10} , \mathbf{H}_{11} , \mathbf{H}_2 , \mathbf{H}_3 , \mathbf{H}_4 , \mathbf{H}_5 , \mathbf{H}_6 , \mathbf{H}_7 and \mathbf{H}_8 are 8×8 matrices. The explicit form of these matrices can be found in Ref. 16. At the initial time, $t = 0$, the disturbance vector is denoted as

$$\mathbf{A}(x, y, z, 0) = \mathbf{A}_0(x, y, z). \quad (3)$$

The boundary conditions are as follows:

$$\begin{aligned} y = 0 : \quad & u = v = w = \theta = 0; \\ y \rightarrow \infty : \quad & |A_j| \rightarrow 0 \quad (j = 1, \dots, 8). \end{aligned} \quad (4)$$

These boundary conditions correspond to the no-slip condition and zero temperature disturbance on the wall, and all disturbances decaying to zero far outside the boundary layer.

III. Solution of the Initial-Value Problem

The problem is solved using a Fourier transform with respect to the streamwise coordinate, x , a Fourier transform with respect to the spanwise coordinate, z , and a Laplace transform with respect to time, t . The inverse Laplace transform of $\mathbf{A}_{p\alpha\beta}$, the solution of the transformed equations, is determined by poles (relevant to the discrete spectrum) and by branch cuts (relevant to the continuous spectrum). By integrating along an appropriate contour in the complex plane (see Ref. 16), the inverse Laplace transform can be written as a sum of integrals along the sides, γ^+ and γ^- , of each branch cut and a sum of residues resulting from the

poles, i.e.,

$$\mathbf{A}_{\alpha\beta} = -\frac{1}{2\pi i} \sum_m \left(\int_{\gamma_m^+} \mathbf{A}_{p\alpha\beta} e^{pt} dp + \int_{\gamma_m^-} \mathbf{A}_{p\alpha\beta} e^{pt} dp \right) + \sum_n \text{Res}_n (\mathbf{A}_{p\alpha\beta} e^{pt}). \quad (5)$$

Details of the problem formulation and solution can be found in Ref. 16.

A. Discrete and continuous spectrum

The behavior of the spectrum must be understood in order to compute the inverse Fourier transform. To illustrate features of the spectrum, a boundary layer over a sharp cone at zero angle of attack is considered. The length scale is $L^* = \sqrt{\mu_e^* x^* / \rho_e^* U_e^*}$ and the Reynolds number is $\text{Re} = \sqrt{\rho_e^* U_e^* x^* / \mu_e^*}$, where U_e^* , ρ_e^* and μ_e^* are respectively the streamwise mean velocity, density and viscosity at the boundary layer edge, and x^* refers to a dimensional quantity. The coordinate x^* is measured from the front tip of the cone. Using the Lees-Dorodnitsyn transformation,²⁵ the conical problem with boundary layer profiles for a flat plate is solved. Accordingly, all conical results presented hereafter can be adjusted to the flat plate boundary layer by dividing the parameters Re , α , β and ω by $\sqrt{3}$. All numerical results are for the case of 2D mean flow. To maintain consistency with the 2D problem analyzed in Ref. 15, the following parameter values are chosen: $M = 5.6$, $\text{Re} = 1219.5$, $\text{Pr} = 0.7$, $\gamma = 1.4$, with an adiabatic wall and stagnation temperature $T_0 = 470$ K, where M is the Mach number at the boundary layer edge, Pr is the Prandtl number and γ is the specific heat ratio.

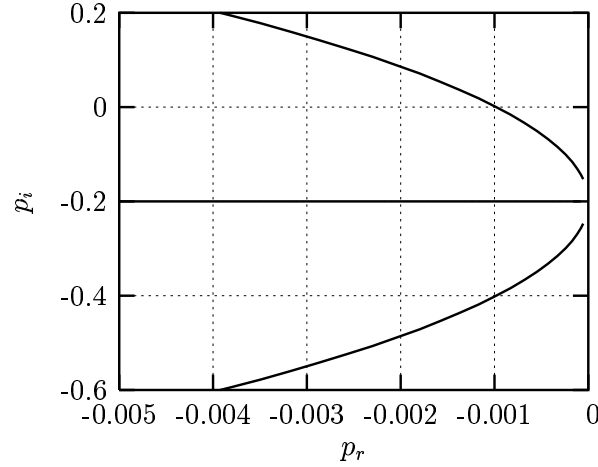


Figure 1. Branch cuts of the continuous spectrum in the complex plane, $p = -i\omega$, for $M = 5.6$, $\text{Re} = 1219.5$, $\alpha = 0.2$ and $\beta = 0.14$.

Discrete modes are given by the poles' contribution to the inverse Laplace transform, i.e., the residues shown in Eq. (5). Continuous modes are given by the branch cuts' contribution to the inverse Laplace transform, i.e., the integrals shown in Eq. (5). There are five branch cuts associated with the continuous spectrum. Three of these branch cuts are shown in Fig. 1 for $\alpha = 0.2$ and $\beta = 0.14$, where α and β are respectively the streamwise and spanwise wave numbers. The branch points of the upper and lower branch cuts represent fast and slow acoustic modes that travel downstream with the respective phase speeds $c = 1 \pm \sqrt{1 + \beta^2 / \alpha^2} / M$. The horizontal branch cut in Fig. 1 has a finite limiting point and is interpreted as an entropy branch, where the entropy disturbances are propagating with a phase speed of $c = 1$. Two of the five branch cuts are not shown in Fig. 1. These two branch cuts are interpreted as vorticity branches, where the vorticity disturbances are propagating with a phase speed of $c = 1$. Both of these vorticity branches overlap the entropy branch shown in Fig. 1. If an eigenvalue belongs to the discrete spectrum, then the associated

eigenfunction decays exponentially outside the boundary layer ($y \rightarrow \infty$). Eigenfunctions associated with continuous modes oscillate outside the boundary layer. Details regarding the discrete spectrum and the various regions of the continuous spectrum can be found in Ref. 16.

IV. Biorthogonal System of Eigenfunctions

It is possible to express a solution of the initial-value problem as an expansion in the biorthogonal eigenfunction system $\{\mathbf{A}_\omega, \mathbf{B}_\omega\}$. The vector \mathbf{A}_ω is a solution of the direct problem, and the vector \mathbf{B}_ω is a solution of the adjoint problem.

Solutions of the direct and adjoint problems belong to the discrete and continuous spectrum. The eigenfunction system $\{\mathbf{A}_\omega, \mathbf{B}_\omega\}$ has an orthogonality relation given as

$$\langle \mathbf{H}_{10} \mathbf{A}_\omega, \mathbf{B}_{\omega'} \rangle \equiv \int_0^\infty (\mathbf{H}_{10} \mathbf{A}_\omega, \mathbf{B}_{\omega'}) dy = \Gamma \Delta_{\omega, \omega'}, \quad (6)$$

where Γ is a normalization constant. $\Delta_{\omega, \omega'}$ is a Kronecker delta if either ω or ω' belong to the discrete spectrum. $\Delta_{\omega, \omega'} = \delta(\omega - \omega')$ is a Dirac delta function if both ω and ω' belong to the continuous spectrum.

It is possible to show that the inverse Laplace transform can be expressed as an expansion in the biorthogonal eigenfunction system¹⁶

$$\mathbf{A}_{\alpha\beta}(y, t) = \sum_\nu c_\nu \mathbf{A}_{\alpha\beta\omega_\nu}(y) e^{-i\omega_\nu t} + \sum_j \int_0^\infty c_j(k) \mathbf{A}_{\alpha\beta\omega_j}(y) e^{-i\omega_j(k)t} dk, \quad (7)$$

where \sum_ν denotes a summation over the discrete spectrum and \sum_j denotes a summation over the continuous spectrum. Using the Fourier transform of the initial disturbance, $\mathbf{A}_{0\alpha\beta}$, as well as the orthogonality relation (Eq. (6)), one can find the coefficients c_ν and c_j . Further details regarding the biorthogonal system of eigenfunctions can be found in Ref. 16.

V. Numerical Study of the Spectrum

Forgoston and Tumin¹⁶ initially studied the spectrum for the mean flow considered in the 2D problem.¹⁵ This set of parameters can be found on page 4 of the present work and will be referred to as Case 1. In the cases that follow (Case 2 - Case 5), the effect of Reynolds number, Mach number and two temperature factors on the spectrum will be studied.

A. Spectrum Overview

There are three types of synchronism that will be discussed. These features will be illustrated using the 2D spectrum. Figure 2 shows numerical results for the eigenvalues of Mode F and Mode S for $\psi = 0^\circ$, where ψ is the angle of disturbance propagation and is given by $\tan \psi = \beta/\alpha$. Included in Fig. 2 are lines of constant phase speed. One of these is a line of phase speed $c = 1$, the speed at which entropy and vorticity disturbances travel. The other lines are associated with the 2D fast acoustic mode (FA mode) and slow acoustic mode (SA mode). The 2D fast and slow acoustic modes travel with phase speed $c = 1 \pm 1/M_e$ (as mentioned in section III, these phase speeds are relevant at the branch points).

The first feature involves the synchronism of Mode F and Mode S respectively with the fast and slow acoustic modes. As seen in Fig. 2, these synchronism occur for a wavenumber $\alpha \rightarrow 0$. The second feature is the synchronism of Mode F with the entropy and vorticity modes of the phase speed $c = 1$. Figure 2 shows that this synchronism occurs at $\alpha \approx 0.2$. One can also see in Fig. 2 that there is a jump in ω_i associated with this synchronism. The third synchronism is that of Mode F with Mode S. As can be seen in Fig. 2, this synchronism occurs at $\alpha \approx 0.23$. One can also see that for this choice of parameters, Mode S becomes more unstable while Mode F becomes more stable. Details of these synchronism along with details regarding the presence of the jump discontinuity and the mode branching can be found in Refs. 16 and 26. The results of a comprehensive study of the effect of Reynolds number, Mach number and the two temperature factors on the spectrum can be found in Ref. 26.

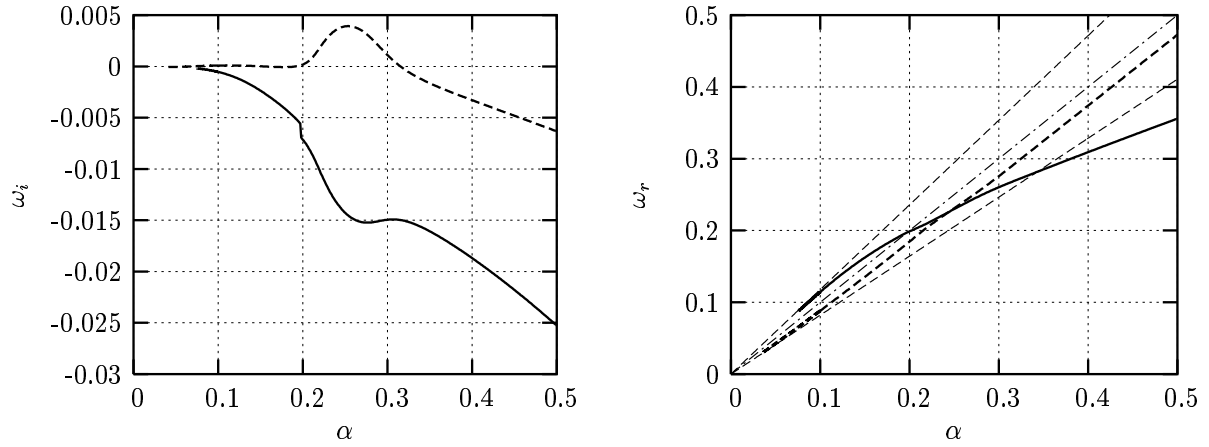


Figure 2. Eigenvalues for Mode F (bold solid line) and Mode S (bold dashed line) for $\psi = 0^\circ$ for $M = 5.6$ and $Re = 1219.5$. The dashed-dotted line corresponds to the line of phase speed $c = 1$. The upper dashed line is associated with the $\psi = 0^\circ$ FA mode, while the lower dashed line is associated with the $\psi = 0^\circ$ SA mode.

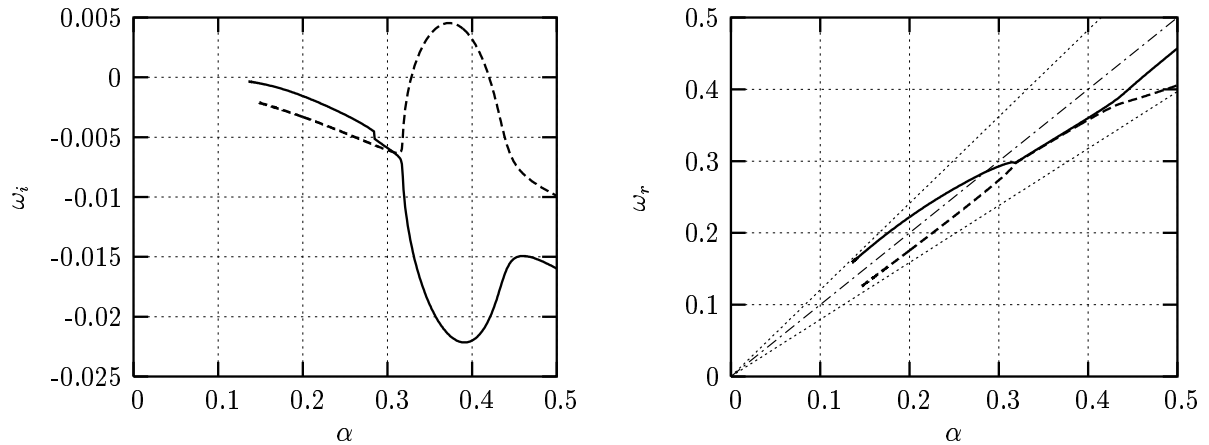


Figure 3. Eigenvalues for Mode F (bold solid line) and Mode S (bold dashed line) for $\psi = 30^\circ$ for $T_f = 0.25$. The dashed-dotted line corresponds to the line of phase speed $c = 1$. The upper dotted line is associated with the $\psi = 30^\circ$ FA mode, while the lower dotted line is associated with the $\psi = 30^\circ$ SA mode.

One can see from this study that the parameter changes do not affect the fundamental features of the spectrum (the three types of synchronism). Significant differences can be found for the various cases with regards to the synchronism location, size of the jump in ω_i , type of topological branching, etc. In particular, there is an interesting change in topology associated with the Mode F - Mode S synchronism when the temperature factor, $T_f = T_w/T_{ad}$, where T_w is the wall temperature and T_{ad} is the adiabatic wall temperature, is changed from $T_f = 1.0$ (Case 1) to $T_f = 0.25$ (Case 5).

Figures 3 and 4 show the eigenvalue curves for Mode F and Mode S for $\psi = 30^\circ$ and $\psi = 45^\circ$ respectively. As in Case 1, there is a synchronism between the 2D Mode F and Mode S. For Case 1, the real part of the eigenvalue curves follow what Mack referred to as Pattern A, one of two standard patterns (Ref. 18, 19, pp. 11-22 - 11-23, pp. 12-26 - 12-27). However, for $T_f = 0.25$ and $\psi = 0^\circ$, the pattern has changed to Pattern B. As with Case 1 though, the synchronism is associated with Mode S becoming more unstable and Mode

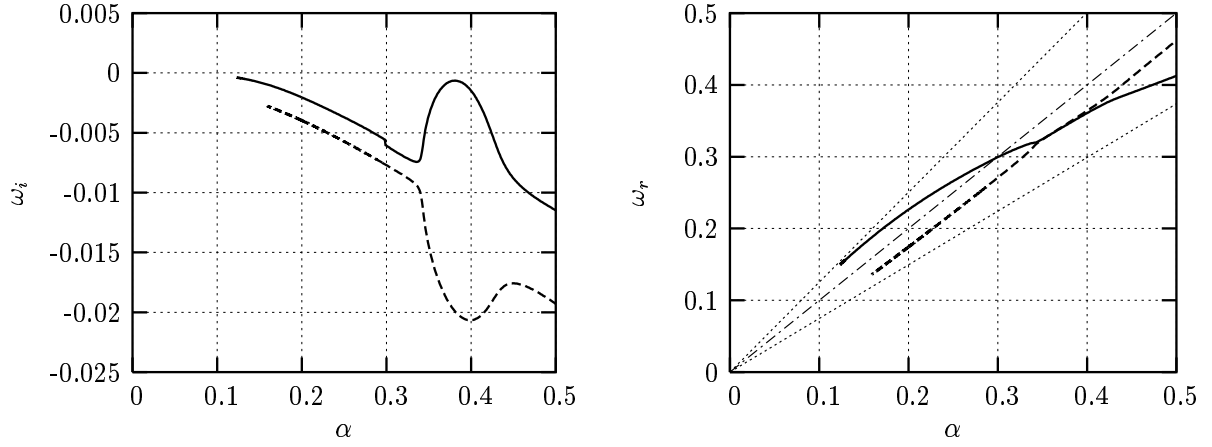


Figure 4. Eigenvalues for Mode F (bold solid line) and Mode S (bold dashed line) for $\psi = 45^\circ$ for $T_f = 0.25$. The dashed-dotted line corresponds to the line of phase speed $c = 1$. The upper dotted line is associated with the $\psi = 45^\circ$ FA mode, while the lower dotted line is associated with the $\psi = 45^\circ$ SA mode.

F becoming more stable. As seen in Fig. 3, Pattern B with the associated Mode S instability continues for a disturbance with a propagation angle of $\psi = 30^\circ$. For the parameter values used in Case 1, it was seen that the synchronism between Mode F and Mode S continued to occur at higher angle of disturbance propagation, but with no Mode S instability accompanying the synchronism. For even higher angles, the synchronism ceased. There is a much different behavior for $T_f = 0.25$. Figure 4 shows that, as with Case 1, the synchronism between Mode F and Mode S exists for a disturbance propagating at $\psi = 45^\circ$. However, in contrast to Case 1, Mode F becomes more unstable (although it is not unstable), while Mode S becomes more stable. Furthermore, one can see that the pattern has returned to Pattern A. At higher angles of disturbance propagation, there is no synchronism between Mode F and Mode S (as in Case 1).

VI. Receptivity to a Temperature Spot

As an example of a specific initial disturbance, Forgoston and Tumin¹⁷ considered a temperature spot localized at a distance Y_0 from the wall. For the 3D initial-value problem, this disturbance will have the form

$$\theta(x, y, z) = \delta(x)\delta(y - Y_0)\delta(z) \quad \text{at } t = 0. \quad (8)$$

The orthogonality condition given by Eq. (6) allows one to determine the weights of the modes generated by the temperature spot. For Mode F and Mode S, the weight is given by

$$c(\alpha, \beta) = \frac{\langle \mathbf{H}_{10} \mathbf{A}_{0\alpha\beta}, \mathbf{B}_\omega \rangle}{\langle \mathbf{H}_{10} \mathbf{A}_\omega, \mathbf{B}_\omega \rangle}, \quad (9)$$

where $\omega(\alpha, \beta)$ corresponds to the eigenvalue for the mode of interest. For a temperature spot of the form given by Eq. (8), it is possible to use the definition of the matrix \mathbf{H}_{10} to obtain from Eq. (9) the expression

$$c(\alpha, \beta) = \frac{H_{10}^{35}(Y_0) \mathbf{B}_{\omega 3}(Y_0) + H_{10}^{65}(Y_0) \mathbf{B}_{\omega 6}(Y_0)}{\langle \mathbf{H}_{10} \mathbf{A}_\omega, \mathbf{B}_\omega \rangle}, \quad (10)$$

where H_{10}^{ij} denotes the (i, j) element of \mathbf{H}_{10} .

The coefficient $c(\alpha, \beta)$ depends on the normalization of the eigenfunction \mathbf{A}_ω . However, the product $c(\alpha, \beta) \mathbf{A}_\omega$ is independent of the choice of normalization. When the inverse Fourier transform of the stream-

wise velocity disturbance, u , is considered, the eigenfunction is normalized so that the maximum value of u is 1. However, for the choice of parameters being used, there are two local maxima of the eigenfunction. Therefore, a choice has been made to normalize the eigenfunction so that the value of the inner maximum is 1 (i.e. \mathbf{A}_ω is normalized as $u_{\max} = \text{inner maximum of } u(y) = 1$). The normalized value of the outer maximum may be greater than 1. With this normalization, c is the amplitude of the maximum streamwise velocity disturbance u_{\max} associated with the appropriate mode.

As a limiting case, as $\beta \rightarrow 0$, one obtains the receptivity coefficient associated with the 2D initial-value problem.¹⁵ It is this 2D coefficient that will be used in the following section to find the 2D inverse Fourier transform.

VII. Inverse Fourier Transform - 2D

The 2D inverse Fourier transform of the streamwise velocity component, u , of the disturbance vector, \mathbf{A} , is given as

$$\int_{-\infty}^{\infty} c(\alpha) u(\alpha, y) e^{i(\alpha x - \omega(\alpha)t)} d\alpha, \quad (11)$$

where the coefficient $c(\alpha)$ is, for this example, the amplitude of the maximum streamwise velocity component u_{\max} . Details of the 2D inverse Fourier transform computation for the Mode F and Mode S wave packets can be found in Ref. 17. Additionally, one can find in Ref. 17 a comparison of the Mode S computed inverse Fourier transform with an asymptotic approximation of the Fourier integral. The asymptotic approximation is found using a 2nd order Taylor series expansion of ω_α within the framework of the method of steepest descent and is given as

$$c(\alpha_{\max}) u(\alpha_{\max}, y) \sqrt{\frac{2\pi}{it \left(\frac{\partial^2 \omega}{\partial \alpha^2}\right)_{\max}}} \times \exp\left(i\alpha_{\max}x + \frac{i(x - x_{\max})^2}{2t \left(\frac{\partial^2 \omega}{\partial \alpha^2}\right)_{\max}} - i\omega_{\max}t\right), \quad (12)$$

where α_{\max} is a point near the saddle point, α^* . Using numerical results, the various quantities found in Eq. (12) can be determined, and these values can be used to compare the computed inverse Fourier transform with the asymptotic approximation of the transform.

Figure 5 compares the wave packet found for $Y_0 = 8.9$ and $t = 500$ at the slice $y = 2.02$ with the asymptotic approximation at $t = 500$ given by Eq. (12).

Overall, the asymptotic representation provides a good approximation to the computed wave packet. However, the ‘‘tails’’ of the two wave packets do not agree very well. This is particularly true for the front edge of the wave packet, whose behavior is dictated by low values of the wave number α .

A. Asymptotic approximation with numerical computation of the saddle point

In an attempt to improve the asymptotic approximation of the wave packet at the ‘‘tails’’ of the wave packet, the location of the saddle point in the complex α plane is numerically computed. To find the saddle point, α^* , at a prescribed x/t , let $\phi(\alpha) = \alpha x/t - \omega(\alpha)$ and derive the following:

$$\left(\frac{\partial \phi}{\partial \alpha}\right)^* = \frac{x}{t} - \frac{\partial \omega}{\partial \alpha} = 0. \quad (13)$$

Therefore, the following relationships must be satisfied at α^* :

$$\frac{x}{t} = \frac{\partial \omega_r}{\partial \alpha} \quad \text{and} \quad 0 = \frac{\partial \omega_i}{\partial \alpha}. \quad (14)$$

Using the method of steepest descent, the asymptotic representation of the inverse Fourier transform is given as:

$$c(\alpha^*) u(\alpha^*, y) \sqrt{\frac{2\pi}{it \left(\frac{\partial^2 \omega}{\partial \alpha^2}\right)^*}} \times \exp(i\alpha^*x - i\omega^*t) \quad (15)$$

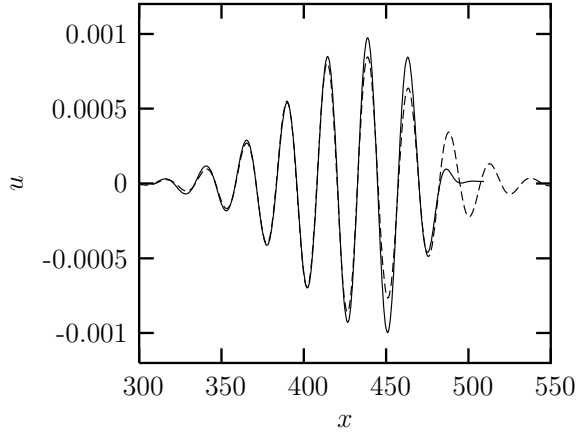


Figure 5. Comparison of computed integral (solid line) with the asymptotic approximation (using 2nd order Taylor series expansion of $\omega(\alpha)$) (dashed line) for the streamwise velocity disturbance, u , at $y = 2.02$ for $t = 500$.

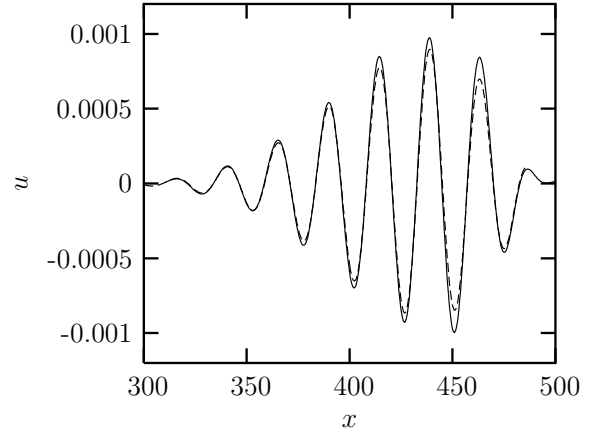


Figure 6. Comparison of computed integral (solid line) with the asymptotic approximation (using numerically computed saddle point values) (dashed line) for the streamwise velocity disturbance, u , at $y = 2.02$ for $t = 500$.

(Note that Eq. (15) is the same as Eq. (12) with $x = x_{\max}$ and all of the “max”-values replaced by “saddle point (*)”-values).

The quantity $\left(\frac{\partial\omega}{\partial\alpha}\right)$ can be found using the eigenfunctions of the direct and adjoint problems. Taking the derivative with respect to α of the direct problem, $\frac{d\mathbf{A}}{dy} = \mathbf{H}_0\mathbf{A}$, leads to the following:

$$\frac{d}{dy} \frac{\partial\mathbf{A}}{\partial\alpha} = \frac{\partial\mathbf{H}_0}{\partial\alpha} \mathbf{A} + \frac{\partial\mathbf{H}_0}{\partial\omega} \frac{\partial\omega}{\partial\alpha} \mathbf{A} + \mathbf{H}_0 \frac{\partial\mathbf{A}}{\partial\alpha}. \quad (16)$$

Using the solvability condition of the inhomogeneous problem, it is possible to show that

$$\frac{\partial\omega}{\partial\alpha} = -\frac{\left\langle \frac{\partial\mathbf{H}_0}{\partial\alpha} \mathbf{A}, \mathbf{B} \right\rangle}{\left\langle \frac{\partial\mathbf{H}_0}{\partial\omega} \mathbf{A}, \mathbf{B} \right\rangle}. \quad (17)$$

Using Eqs. (14) and (17), α^* , ω^* and $\left(\frac{\partial\omega}{\partial\alpha}\right)^*$ are calculated with Newton’s iteration method. Finite differences are then used to find $\left(\frac{\partial^2\omega}{\partial\alpha^2}\right)^*$. Figure 6 compares the computed wave packet found for $Y_0 = 8.9$ and $t = 500$ at the slice $y = 2.02$ with the asymptotic approximation at $t = 500$ given by Eq. (15) using the saddle point values. There is now excellent agreement across the entire wave packet.

The inverse Fourier transform has been computed for the streamwise velocity disturbance u and the temperature disturbance θ for $t = 500$, $t = 1000$ and $t = 1500$ for Cases 1-5. The computational results have been compared to the asymptotic approximation of the Fourier integral and can be found in Ref. 26.

When using the method of steepest descent, it is not enough to simply compute the location of the saddle point. One must also demonstrate that the original contour path of integration can be deformed to pass through the saddle point. Figure 7 shows contours of the $\text{Real}\{\phi(\alpha)\}$ (solid lines) and the $\text{Imag}\{\phi(\alpha)\}$ (dashed lines) in the complex α plane, where $\phi(\alpha) = \alpha x/t - \omega(\alpha)$. Inspection of Fig. 7 shows that as one integrates along the real axis ($\alpha_i = 0$), it is possible to first deform the path onto a level curve of the $\text{Real}\{\phi(\alpha)\}$ (where the phase is constant), then to pass through the saddle point along the lines of steepest descent, and finally to return to the real axis along a level curve of the $\text{Real}\{\phi(\alpha)\}$.

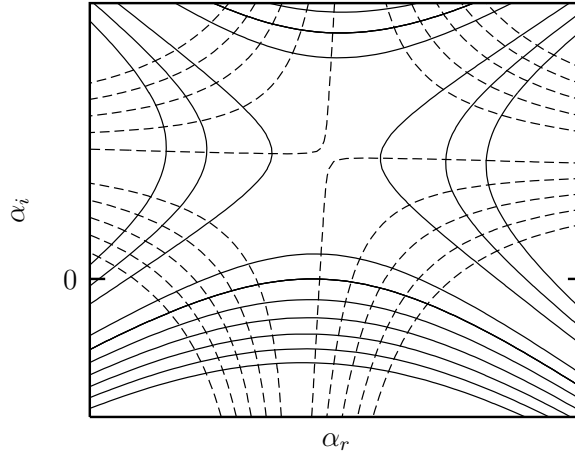


Figure 7. Contours of the $\text{Real}\{\phi(\alpha)\}$ (solid lines) and the $\text{Imag}\{\phi(\alpha)\}$ (dashed lines) in the complex α plane.

VIII. Inverse Fourier Transform - 3D

It was shown in Ref. 17 that it was necessary to deform the path of integration of the 2D inverse Fourier transform for Mode F, but not for Mode S. Each inversion of the Fourier integral must be accompanied by an analysis of the spectrum to find a suitable integration path. In order to perform the double integration of the 3D inverse Fourier transform, it is again necessary to understand the features of the spectrum so that an appropriate path of integration is used. Due to the complexities associated with the 3D spectrum, an asymptotic approximation of the Fourier integral will be used to compute the 3D wave packets.

For the streamwise velocity disturbance, u , the 3D inverse Fourier transform is given as

$$\int_{-\infty}^{\infty} \int_{-\infty}^{\infty} c(\alpha, \beta) u(\alpha, \beta, y) e^{i(\alpha x + \beta z - \omega(\alpha, \beta)t)} d\alpha d\beta. \quad (18)$$

As in the 2D case, Eq. (18) can be transformed using a symmetry argument. Using the direct and complex conjugate matrix operator equations, when α is replaced by $-\alpha$, i.e. when $\alpha \rightarrow -\alpha$, it can be shown that $\beta \rightarrow -\beta$, $\omega \rightarrow -\bar{\omega}$, $c \rightarrow \bar{c}$, and $u \rightarrow \bar{u}$, where the over-bar stands for complex conjugate. Therefore, Eq. (18) can be rewritten as:

$$\int_{-\infty}^{\infty} \int_{-\infty}^{\infty} c(\alpha, \beta) u(\alpha, \beta, y) e^{i(\alpha x + \beta z - \omega(\alpha, \beta)t)} d\alpha d\beta = \quad (19a)$$

$$2 \int_0^{\infty} \int_0^{\infty} \text{Real}\{c(\alpha, \beta) u(\alpha, \beta, y) e^{i(\alpha x + \beta z - \omega(\alpha, \beta)t)}\} d\alpha d\beta$$

$$+ 2 \int_0^{\infty} \int_0^{\infty} \text{Real}\{c(\alpha, -\beta) u(\alpha, -\beta, y) e^{i(\alpha x - \beta z - \omega(\alpha, -\beta)t)}\} d\alpha d\beta. \quad (19b)$$

As was done for the 2D case (see Ref. 17), the factor of 2 will be ignored.

At a first glance of Eq. (19b), it is tempting to think that there are two saddle points. The first saddle point, associated with the first double integral, must satisfy the following relations:

$$\begin{aligned}\frac{x}{t} &= \frac{\partial \omega_r(\alpha, \beta)}{\partial \alpha} & \text{and} & & 0 &= \frac{\partial \omega_i(\alpha, \beta)}{\partial \alpha}; \\ \frac{z}{t} &= \frac{\partial \omega_r(\alpha, \beta)}{\partial \beta} & \text{and} & & 0 &= \frac{\partial \omega_i(\alpha, \beta)}{\partial \beta}.\end{aligned}\quad (20)$$

The second saddle point, associated with the second double integral, must satisfy the following relations:

$$\begin{aligned}\frac{x}{t} &= \frac{\partial \omega_r(\alpha, -\beta)}{\partial \alpha} & \text{and} & & 0 &= \frac{\partial \omega_i(\alpha, -\beta)}{\partial \alpha}; \\ \frac{z}{t} &= \frac{\partial \omega_r(\alpha, -\beta)}{\partial \beta} & \text{and} & & 0 &= \frac{\partial \omega_i(\alpha, -\beta)}{\partial \beta}.\end{aligned}\quad (21)$$

Using the symmetry transformations along with properties of complex conjugation, it can be shown that Eq. (21) can be rewritten as

$$\begin{aligned}\frac{x}{t} &= -\frac{\partial \omega_r(\alpha, \beta)}{\partial \alpha} & \text{and} & & 0 &= \frac{\partial \omega_i(\alpha, \beta)}{\partial \alpha}; \\ \frac{z}{t} &= \frac{\partial \omega_r(\alpha, \beta)}{\partial \beta} & \text{and} & & 0 &= \frac{\partial \omega_i(\alpha, \beta)}{\partial \beta}.\end{aligned}\quad (22)$$

However, it can be shown numerically that no saddle point satisfies the relations given in Eq. (22), unless $x = 0$ and $z = 0$. Therefore, there is only one saddle point, and it is associated with the first double integral of Eq. (19b).

One can follow Gaster²⁷ to find the asymptotic representation of the integral given by Eq. (18). For a fixed β , Eq. (18) becomes

$$\int_{-\infty}^{\infty} e^{i\beta z} \int_{-\infty}^{\infty} e^{it(\alpha \frac{x}{t} - \omega(\alpha, \beta))} d\alpha d\beta. \quad (23)$$

The asymptotic representation of the inner integral in Eq. (23) is known from the 2D case, and substitution of this representation leads to the following:

$$\sqrt{\frac{2\pi}{i}} \int_{-\infty}^{\infty} \frac{e^{it(\alpha^*(\beta) \frac{x}{t} + \beta \frac{z}{t} - \omega(\alpha^*(\beta), \beta))}}{\sqrt{t \frac{\partial^2 \omega}{\partial \alpha^2}(\alpha^*, \beta)}} d\beta. \quad (24)$$

If one lets

$$\phi(\alpha^*, \beta) = i \left(\alpha^*(\beta) \frac{x}{t} + \beta \frac{z}{t} - \omega(\alpha^*(\beta), \beta) \right), \quad (25)$$

and expands ϕ about β^* so that

$$\phi(\alpha^*, \beta) \approx i \left[\phi(\alpha^*, \beta^*) + \frac{(\beta - \beta^*)^2}{2} \phi''(\alpha^*, \beta^*) \right], \quad (26)$$

then Eq. (23) can be written as:

$$\sqrt{\frac{2\pi}{it}} \frac{e^{it(\alpha^* x + \beta^* z - \omega(\alpha^*, \beta^*))}}{\sqrt{\frac{\partial^2 \omega}{\partial \alpha^2}(\alpha^*, \beta^*)}} \times \int_{-\infty}^{\infty} e^{it \frac{(\beta - \beta^*)^2}{2} \left(\frac{\partial^2 \omega}{\partial \beta^2} + 2 \frac{\partial^2 \omega}{\partial \alpha \partial \beta} \left(\frac{\partial \alpha}{\partial \beta} \right) + \frac{\partial^2 \omega}{\partial \alpha^2} \left(\frac{\partial \alpha}{\partial \beta} \right)^2 \right)^*} = \quad (27a)$$

$$\frac{2\pi}{it} \frac{e^{it(\alpha^* x + \beta^* z - \omega(\alpha^*, \beta^*))}}{\sqrt{\left(\frac{\partial^2 \omega}{\partial \alpha^2} \frac{\partial^2 \omega}{\partial \beta^2} - \left(\frac{\partial^2 \omega}{\partial \alpha \partial \beta} \right)^2 \right)^*}}. \quad (27b)$$

The asymptotic representation of the inverse Fourier transform given by Eq. (27b) can be derived more generally using a transformation of variables.^{28,29} Starting with Eq. (18) with ϕ given as $\phi(\alpha, \beta) = \alpha x + \beta z - \omega(\alpha, \beta) t$, ϕ may be approximated as:

$$\phi(\alpha, \beta) \approx \phi^* + \frac{(\alpha - \alpha^*)^2}{2} \phi_{\alpha\alpha}^* + (\alpha - \alpha^*)(\beta - \beta^*) \phi_{\alpha\beta}^* + \frac{(\beta - \beta^*)^2}{2} \phi_{\beta\beta}^*, \quad (28)$$

where the α and β subscripts refer to first and second partial derivatives.

Using the change of variables

$$g = (\alpha - \alpha^*), \quad h = (\beta - \beta^*),$$

$$\xi = g + \frac{\phi_{\alpha\beta}}{\phi_{\alpha\alpha}} h, \quad \eta = h, \quad (29)$$

Eq. (18) is transformed to the following:

$$\int_{-\infty}^{\infty} \int_{-\infty}^{\infty} e^{\frac{t}{2} \left(\phi_{\alpha\alpha} \xi^2 + \frac{(\phi_{\alpha\alpha} \phi_{\beta\beta} - \phi_{\alpha\beta}^2)}{\phi_{\alpha\alpha}} \eta^2 \right)} d\xi d\eta. \quad (30)$$

The integral given in Eq. (30) is an iterated integral where each integral is Gaussian. Evaluation of the iterated integral results in the asymptotic representation of the Fourier integral given by Eq. (27b).

The saddle point (α^*, β^*) and the various derivatives at the saddle point used in Eq. (27a) are numerically computed. Using the asymptotic approximation of the 3D inverse Fourier transform, the Mode S wave packet is calculated for various times. Figure 8(a) is a surface plot of the streamwise velocity disturbance, u , taken at the slice $y = 2.02$ for $Y_0 = 8.9$ and $t = 500$. Figure 8(b) is a rotation of Fig. 8(a) in order to see the underside of the wave packet. To have a clearer sense of the amplitude values, Fig. 8(c) shows contours of u for $y = 2.02$, $Y_0 = 8.9$, and $t = 500$. Figures 9(a), 9(b) and 9(c) show similar comparisons for $t = 1000$. It is clear from these figures that the wave packet is moving downstream in time. The wave packet is also spreading out in both the streamwise and spanwise directions, and the amplitude is increasing with the increase in time. Figures 8(a) and 9(a) also show that the wave packet for these two choices of time is essentially 2D.

Additionally, the inverse Fourier transform has been found for the streamwise velocity disturbance and the temperature disturbance for $t = 500$ and $t = 1000$ for Cases 2-4. These results can be found in Ref. 26.

IX. Conclusions

The previously solved 2D and 3D initial-value problems for disturbances propagating in a compressible boundary layer flow were used along with features of the discrete and continuous spectrum to study the evolution of wave packets for two discrete modes, Mode F and Mode S. The biorthogonal eigenfunction system provides a method for the determination of the weights of individual modes given a specific initial disturbance.

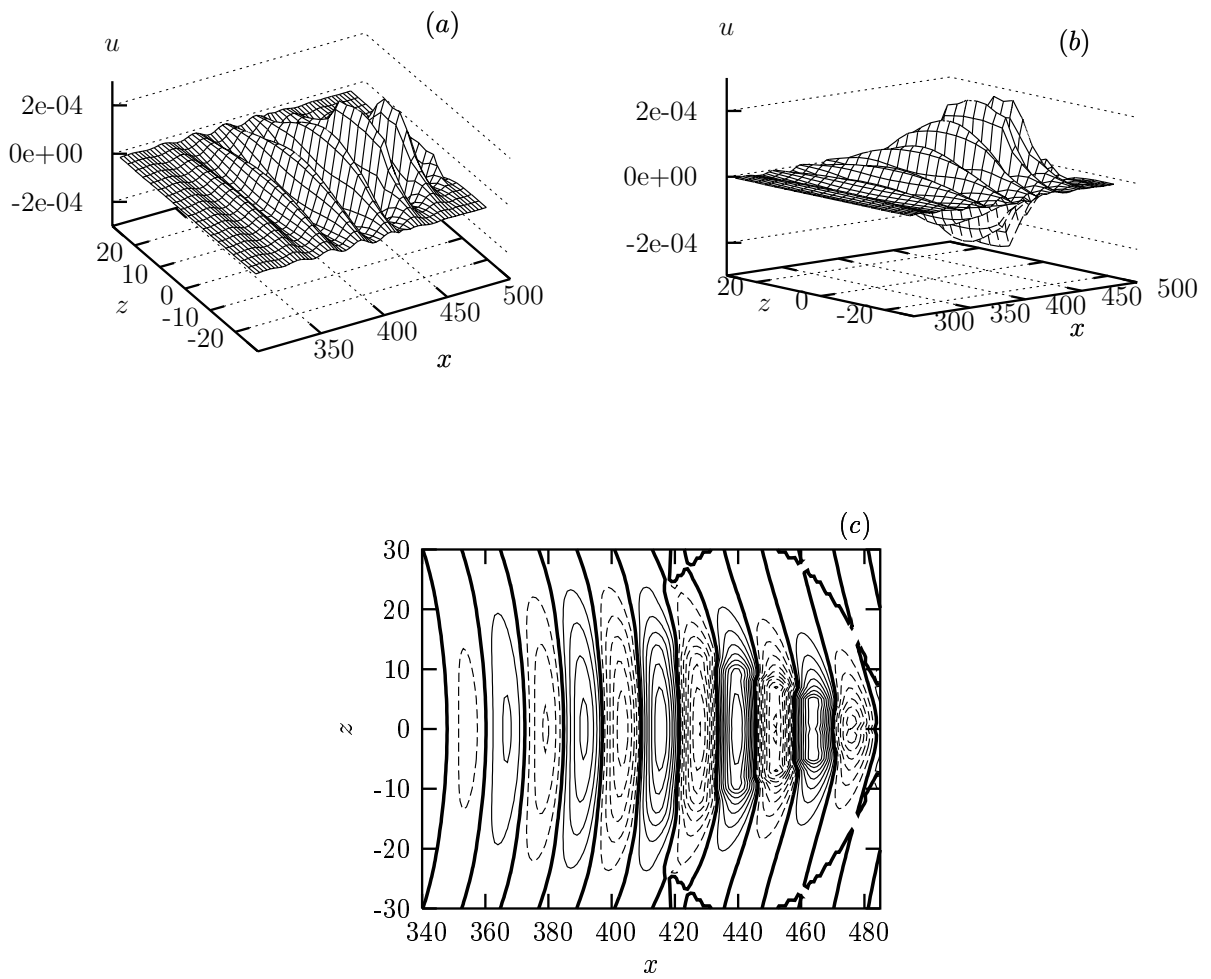


Figure 8. Surface (view 1) (a), surface (view 2) (b) and contours (c) of u for $y = 2.02$, $Y_0 = 8.9$, and $t = 500$. The contour levels in (c) are spaced in increments of 0.000025. The solid contours are positive; the dashed contours are negative; the bold contours are 0.

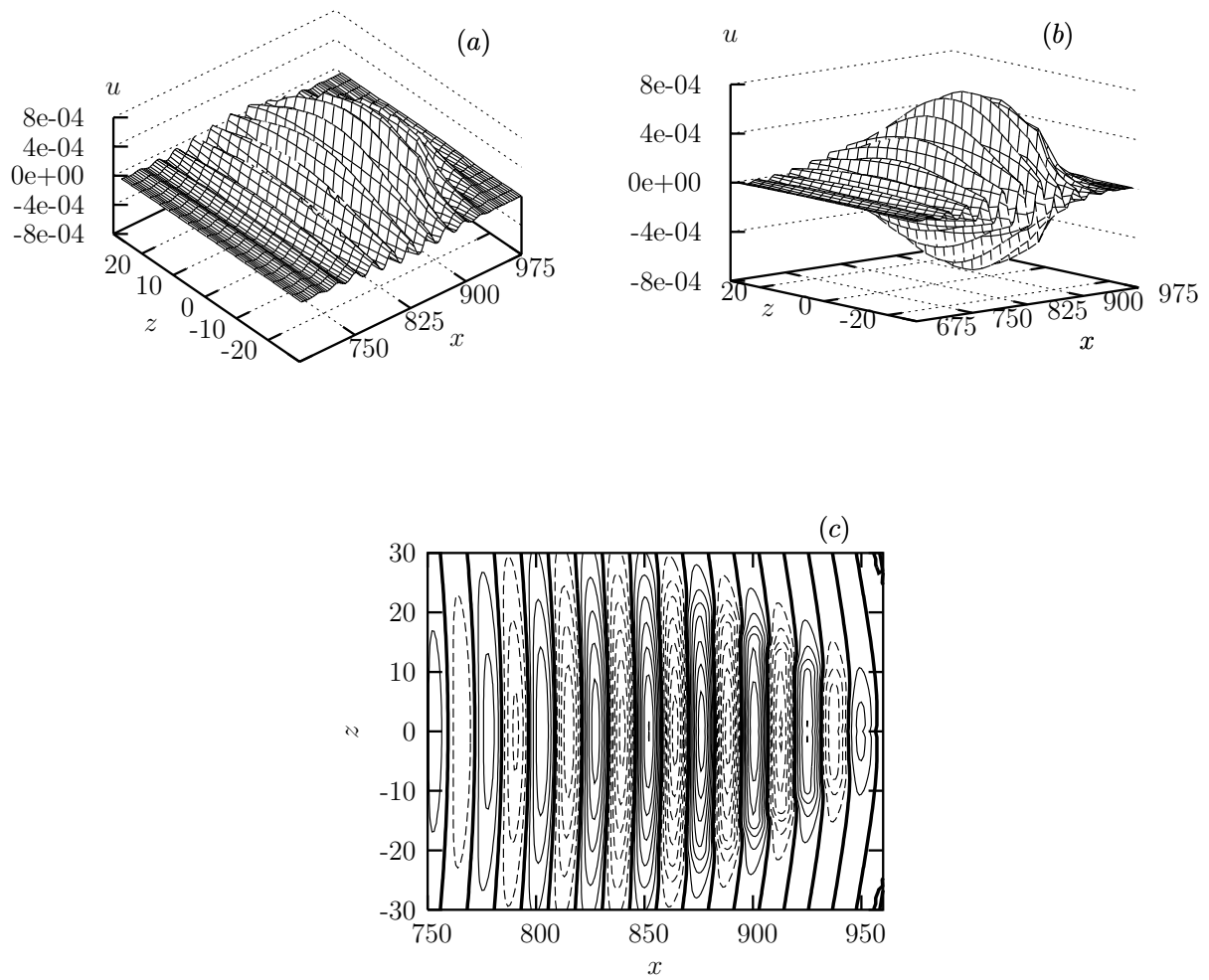


Figure 9. Surface (view 1) (a), surface (view 2) (b) and contours (c) of u for $y = 2.02$, $Y_0 = 8.9$, and $t = 1000$. The contour levels in (c) are spaced in increments of 0.0001. The solid contours are positive; the dashed contours are negative; the bold contours are 0.

Using the specific disturbance of an initial temperature spot, the 2D inverse Fourier transform for both Mode F and Mode S was computed. The results for Mode S were compared with an asymptotic approximation of the Fourier integral. The first approximation used a Taylor series expansion of ω . Generally, this approximation compared favorably with the computed results. However, there is a significant discrepancy at the wave packet “tails”. In the present work, the asymptotic approximation has been improved using numerically computed saddle point values. From a computational point of view, it is much faster to compute the wave packet using the asymptotic approximation with numerically computed saddle point values than it is to compute the inverse Fourier transform.

Furthermore, the full 3D inverse Fourier transform was found. Since the 3D spectrum is so complex, rather than compute the inverse Fourier transform, an asymptotic approximation of the Fourier integral has been used, with numerically computed saddle point values. A key feature of the 3D wave packet is its 2D nature. As discussed in Ref. 16, Mode S is a single discrete mode that corresponds to a single pole in the complex p plane. This single mode is associated with Mack’s first and second modes, and for this set of parameters, the most unstable section of Mode S is associated with Mack’s second mode, whose maximum growth rate is associated with 2D disturbances. Thus, it is not surprising that for sufficiently large time, the 3D wave packet will have a 2D appearance.

In addition, a comprehensive study of the spectrum has been performed. This study includes the effect of Reynolds number, Mach number and temperature factor. Wave packets have been computed for all of these parameter regimes.

Acknowledgments

This work was sponsored by the Air Force Office of Scientific Research, USAF under grant No. FA9550-05-101 monitored by Dr. J. D. Schmisser. The views and conclusions contained herein are those of the authors and should not be interpreted as necessarily representing the official policies or endorsements, either expressed or implied, of the Air Force Office of Scientific Research or the U. S. Government. Additionally, this work was supported by a National Science Foundation graduate student VIGRE fellowship.

References

- ¹Kosinov, A. D., Maslov, A. A., and Shevelkov, S. G., “Experiments on the stability of supersonic laminar boundary layers,” *J. Fluid Mech.*, Vol. 219, 1990, pp. 621–633.
- ²Ladon, D. W. and Schneider, S. P., “Measurements of Controlled Wave Packets at Mach 4 on a Cone at Angle of Attack,” *AIAA Paper 1998-0436*, January 1998.
- ³Schmisser, J. D. and Schneider, S. P., “Receptivity of the Mach-4 Boundary-Layer on an Elliptic Cone to Laser-Generated Localized Free-Stream Perturbations,” *AIAA Paper 1998-0532*, January 1998.
- ⁴Maslov, A. A., Shpiilyuk, A. N., Sidorenko, A. A., and Arnal, D., “Leading-edge receptivity of a hypersonic boundary layer on a flat plate,” *J. Fluid Mech.*, Vol. 426, 2001, pp. 73–94.
- ⁵Zhong, X. and Ma, Y., “Receptivity and Linear Stability of Stetson’s Mach 8 Blunt Cone Stability Experiments,” *AIAA Paper 2002-2849*, June 2002.
- ⁶Ma, Y. and Zhong, X., “Receptivity of a supersonic boundary layer over a flat plate. Part 1. Wave structures and interactions,” *J. Fluid Mech.*, Vol. 488, 2003, pp. 31–78.
- ⁷Ma, Y. and Zhong, X., “Receptivity of a supersonic boundary layer over a flat plate. Part 2. Receptivity to free-stream sound,” *J. Fluid Mech.*, Vol. 488, 2003, pp. 79–121.
- ⁸Egorov, I. V., Fedorov, A. V., and Nechaev, A. V., “Receptivity of Supersonic Boundary Layer on a Blunt Plate to Acoustic Disturbances,” *AIAA Paper 2004-0294*, 2004.
- ⁹Ma, Y. and Zhong, X., “Receptivity of a supersonic boundary layer over a flat plate. Part 3. Effects of different types of free-stream disturbances,” *J. Fluid Mech.*, Vol. 532, 2005, pp. 63–109.
- ¹⁰Egorov, I. V., Fedorov, A. V., and Soudakov, V. G., “Direct Numerical Simulation of Supersonic Boundary Layer Receptivity to Acoustic Disturbances,” *AIAA Paper 2005-0097*, 2005.
- ¹¹Wang, X. and Zhong, X., “Receptivity of a Mach 8.0 Flow Over a Sharp Wedge with Half-Angle 5.3° to Wall Blowing-Suction,” *AIAA Paper 2005-5025*, 2005.
- ¹²Huerre, P. and Rossi, M., “Hydrodynamic instabilities in open flows,” in *Hydrodynamics and Nonlinear Instabilities*, edited by C. Godreche and P. Manneville, Cambridge University Press, 1998, pp. 81–294.
- ¹³Gustavsson, L. H., “Initial-value problem for boundary layer flows,” *Phys. Fluids*, Vol. 22, No. 9, 1979, pp. 1602–1605.
- ¹⁴Salwen, H. and Grosch, C. E., “The continuous spectrum of the Orr-Sommerfeld equation. Part 2. Eigenfunction expansions,” *J. Fluid Mech.*, Vol. 104, 1981, pp. 445–465.
- ¹⁵Fedorov, A. V. and Tumin, A. M., “Initial-Value Problem for Hypersonic Boundary-Layer Flows,” *AIAA J.*, Vol. 41, No. 3, 2003, pp. 379–389.

- ¹⁶Forgoston, E. and Tumin, A. M., “Initial-value problem for three-dimensional disturbances in a compressible boundary layer,” *Phys. Fluids*, Vol. 17, No. 084106, 2005.
- ¹⁷Forgoston, E. and Tumin, A. M., “Three-Dimensional Wave Packet in a Hypersonic Boundary Layer,” *AIAA Paper 2005-0099*, January 2005, [submitted to *Phys. Fluids*].
- ¹⁸Mack, L. M., “Boundary-Layer Stability Theory,” *Jet Propulsion Lab., JPL 900-277, Pasadena, CA*, 1969.
- ¹⁹Mack, L. M., “Special Course on Stability and Transition of Laminar Flow,” *AGARD Report 709*, June 1984.
- ²⁰Fedorov, A. V., “Receptivity of a high-speed boundary layer to acoustic disturbances,” *J. Fluid Mech.*, Vol. 491, 2003, pp. 101–129.
- ²¹Tumin, A. M., “Biorthogonal Eigenfunction System in the Triple-Deck Limit,” *AIAA Paper 2005-0524*, January 2005, [to appear in *Studies in App. Math.*, 2006].
- ²²Tumin, A. M., “Receptivity of compressible boundary layers to three-dimensional wall perturbations,” *AIAA Paper 2006-1110*, 2006, [submitted to *J. Fluid Mech.*].
- ²³Tumin, A. M., “Three-Dimensional Spatial Normal Modes in Compressible Boundary Layers,” *AIAA Paper 2006-1109*, January 2006, [submitted to *J. Fluid Mech.*].
- ²⁴Fedorov, A. V. and Khokhlov, A. P., “Prehistory of Instability in a Hypersonic Boundary Layer,” *Theoret. Comput. Fluid Dynamics*, Vol. 14, 2001, pp. 359–375.
- ²⁵Anderson Jr., J. D., *Hypersonic and High Temperature Gas Dynamics*, AIAA, Inc., 1989.
- ²⁶Forgoston, E., *Initial-Value Problem for Perturbations in Compressible Boundary Layers*, Ph.D. thesis, The University of Arizona, Program in Applied Mathematics, May 2006.
- ²⁷Gaster, M., “The development of three-dimensional wave packets in a boundary layer,” *J. Fluid Mech.*, Vol. 32, 1968, pp. 173–184.
- ²⁸Bleistein, N. and Handelsman, R. A., *Asymptotic Expansions of Integrals*, Dover Publications, Inc., 1986.
- ²⁹Wong, R., *Asymptotic Approximations of Integrals*, Society for Industrial and Applied Mathematics, 2001.